Earth Planet. Sci. Lett. 671 (2025) 119689

Contents lists available at ScienceDirect

Earth and Planetary Science Letters

journal homepage: www.elsevier.com/locate/epsl

High-precision zircon geochronology constrains early Permian exhumation of the deep Adriatic crust in the western Italian Alps

Marco Filippi [a,*], Federico Farina [a], Maria Ovtcharova [b], Fabiola Caso [a,c], Manuel Roda [a], Chiara Benedetta Piloni [a], Michele Zucali [a]

[a] Dipartimento di Scienze della Terra "A. Desio", Università degli Studi di Milano, via Mangiagalli 34, 20133 Milano, Italy

[b] Department of Earth Sciences, University of Geneva, Rue des Maraichers 13, CH-1205 Geneva, Switzerland

[c] Dipartimento di Scienze dell'Ambiente e della Terra, Università degli Studi di Milano-Bicocca, Piazza della Scienza 4, 20126 Milano, Italy

ARTICLE INFO

Editor: Dr A Webb

Keywords:
Adriatic basement
Dent Blanche nappe system
Valpelline series
CA-ID-TIMS U-Pb zircon dating

ABSTRACT

Understanding whether deep crustal exhumation is continuous or occurs through episodic and high-rate pulses is key to linking the tectonic evolution of the continental lithosphere with magmatic processes. However, this remains challenging because of the limited precision of many geochronological methods, especially when resolving closely spaced and ancient metamorphic events. By integrating high-precision U–Pb zircon geochronology with metamorphic P–T estimates from deep crustal migmatitic gneiss, this study quantifies the average exhumation rate of the Valpelline Series within the fossil Permian extensional system of the western Italian Alps.

The migmatitic gneiss of the Valpelline series record a metamorphic transition from conditions of 0.8–1.0 GPa and 870–890 °C (M1) to 0.4–0.6 GPa and 680–760 °C (M2), reflecting cooling and exhumation from deep to middle crustal levels. The changing P–T conditions mark a shift from a late- to post-collisional thermal relaxation regime to extensional tectonics characterized by a higher thermal gradient. CA-ID-TIMS dating constrains this transition to between 294.29 ± 0.38 Ma (M1) and 286.76 ± 0.27 Ma (M2), yielding an exhumation rate of 2.0 ± 1.0 mm/yr restricted to the early Permian and preceding widespread gabbro emplacement at regional scale. The results are consistent with the model that invokes an early Permian transtensional regime across Pangea, marked by high relative plate velocities and a brief duration of less than 20 Myr.

1. Introduction

The exhumation of the deep continental crust in divergent settings is closely linked to high-temperature (HT) metamorphism, partial melting, and volcanic activity. Determining whether exhumation occurs continuously at low rates or episodically at high rates has significant implications for the thermo-mechanical evolution of the lithosphere, as well as for the multiple exchanges between the lithosphere, atmosphere, and biosphere (Harley, 2016; Jiao et al., 2023; Lenardic et al., 2016; Kasbohm et al., 2021).

Petrochronology offers a means to quantify the average rates of tectonic processes (Kohn, 2016; Engi et al., 2017). This approach leverages recent advances in-situ geochronology, which allow dating of accessory and rock-forming minerals (see also Volante et al., 2024). The pressure-temperature (P–T) evolution of metamorphic rocks provides valuable insights into the thermal and burial–exhumation evolution, while the timing (-t) of mineral growth can be correlated with specific P–T stages through the integration of microstructural and mineralogical-chemical criteria (e.g., Hermann and Rubatto, 2003; Whitehouse and Platt, 2003; Rubatto et al., 2006, 2013; Harley et al., 2007; Baldwin and Brown, 2008). Nevertheless, the precision of in-situ dating techniques is often insufficient to resolve short intervals between successive metamorphic events, particularly when these are ancient and closely spaced. For instance, U–Pb zircon dating via laser ablation inductively coupled plasma mass spectrometry (LA-ICP-MS), the most robust and widely used in-situ technique, yields age uncertainties of 1.5–2 % at the 2σ confidence level (Schaltegger et al., 2015; Horstwood et al., 2016).

The limitations of the in-situ techniques have limited impact in active or relatively young convergent settings, such as subduction zones, where the recent timing of events enhances temporal resolution and enables the estimation of high exhumation rates (e.g., Rubatto and Hermann, 2001; Baldwin et al., 2004; Rubatto et al., 2011). Conversely, it becomes critical in divergent settings, where multiple tectonic events

* Corresponding author.
E-mail address: marco.filippi@unimi.it (M. Filippi).

https://doi.org/10.1016/j.epsl.2025.119689
Received 15 February 2025; Received in revised form 16 July 2025; Accepted 11 October 2025
Available online 22 October 2025

are often needed to exhumed the deep crust (e.g., Ring et al., 1999), potentially over long geological times. In such cases, the short time intervals between early stages might be unresolved, impeding efforts to accurately determine exhumation rates. To improve age precision, U–Pb zircon dating by chemical abrasion–isotope dilution–thermal ionization mass spectrometry (CA-ID-TIMS) can achieve uncertainties <0.1 % on $^{238}U/^{206}Pb$ dates. However, this technique generally involves complete dissolution of zircon grains, which results in limited spatial resolution (e.g., Condon et al., 2024). This poses a major limitation for the study of metamorphic rocks, where zircons often preserve complex internal zoning and multiple crystallization domains. As a result and with few exceptions (e.g., Stowell et al., 2022), CA-ID-TIMS U-Pb zircon dating is commonly not applied to metamorphic rocks.

This study aims to show that the superior precision of CA...ID...TIMS dating, when combined with careful textural selection of zircon crystals, provides a more reliable framework for estimating the rates of tectonic processes. The focus is on the Valpelline series, a segment of the Adriatic basement in the western Italian Alps. This deep continental unit is mainly composed of migmatitic gneiss and granulites that record Permian HT metamorphism (Kunz et al., 2018a; Caso et al., 2024a, and references therein). By integrating structural, metamorphic, and geochronological data, we reconstruct its Permian P-T-t evolution and estimate the corresponding average exhumation rate.

2. Geologic setting

2.1. The Adriatic basement in the Alps

The Adriatic basement, exposed at various crustal levels in the Alps, is part of the Permian extensional system that formed after the collapse of the Devonian–Carboniferous Variscan belt (Lardeaux and Spalla, 1991; Schuster and Stüwe, 2008; Kunz et al., 2018a; Roda et al., 2019). Some authors propose that the Adriatic basement experienced a prolonged period of thermal perturbation and magmatism driven by lithospheric extension, either continuous or episodic, characterized by low average exhumation rates extending from the early Permian into the Mesozoic (e.g., Schuster and Stüwe, 2008; Langone et al., 2018; Roda et al., 2019; Smye et al., 2019; Connop et al., 2024). In contrast, other authors relate the magmatic and HT metamorphic evolution of the Adriatic basement to a brief phase of intra-continental transtension that caused a major reorganization of Pangea between 298 and 274 Ma and driven by high plate velocities (Muttoni et al., 2003). This interpretation is supported by the ages of the early Permian intrusive rocks and volcanic sequences within sedimentary basins, which are limited to the 275–289 Ma interval (Schaltegger and Brack, 2007; Quick et al., 2009; Karakas et al., 2019; Boscaini et al., 2025). The transtensional phase ended with a shift in plate kinematics during the late Permian, marked by a decline in magmatic activity and change in sedimentary inputs (Muttoni et al., 2003).

The deepest portion of the Adriatic basement is exposed in the western Alps (Fig. 1; Kunz et al., 2018a and references therein). The HT metamorphic evolution of this section has been deeply investigated, particularly along the Val Strona di Omegna in the Ivrea–Verbano zone (Fig. 1), where a metamorphic field gradient from amphibolite- to granulite-facies conditions is documented (Kunz and White, 2019). The Mafic Complex (Fig. 1), the largest among gabbro intrusive suites in the Adriatic basement, was emplaced within the deepest part of the Ivrea–Verbano zone at 282–286 Ma (Karakas et al., 2019).

Despite well-constrained metamorphic P–T conditions in the Ivrea–Verbano zone, there are divergent interpretations of the tectonic evolution of the deep crust during the Permian. Specifically, questions remain about the causal relationship between gabbro emplacement and

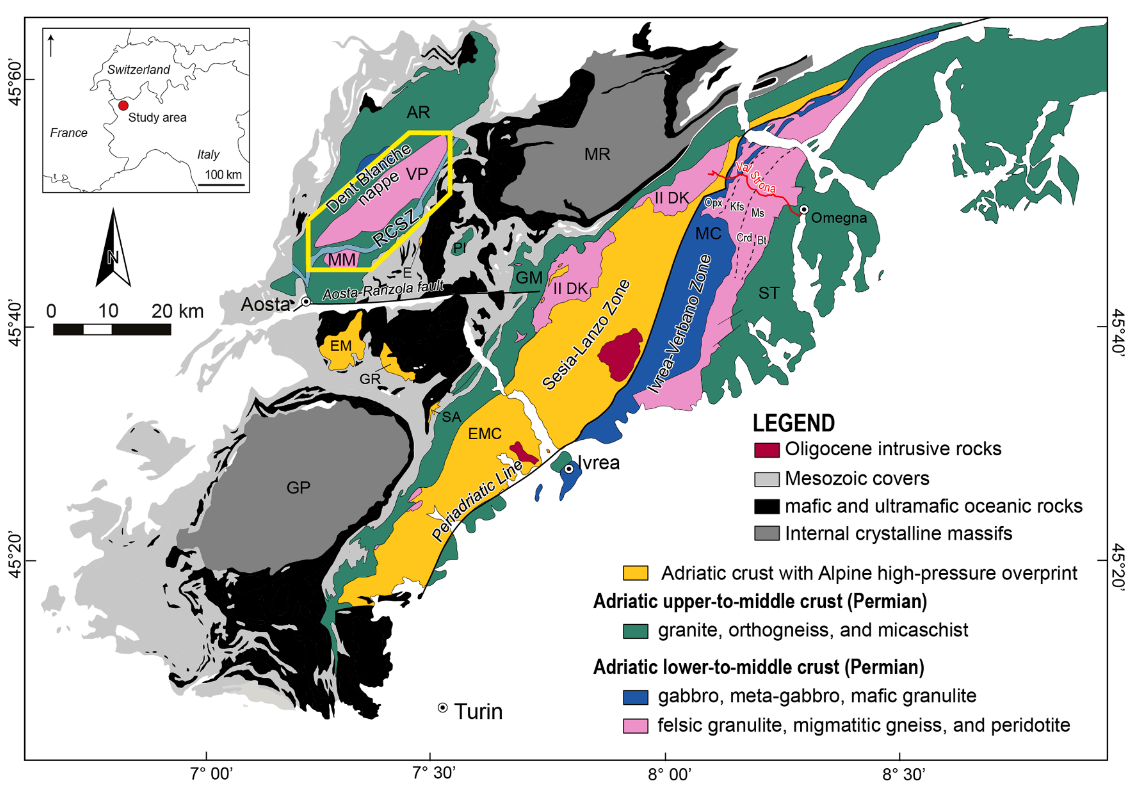

Fig. 1. Simplified tectonic map of the western Italian Alps (modified after Caso et al., 2024b, and references therein; WGS84 geographic coordinates). The metamorphic isograds along the Val Strona di Omegna (in red) are from Kunz and White (2019) and references therein. The area shown in Fig. 2 is outlined in yellow. Labels: AR – Arolla series; E – Etirol Levaz; EMC – Eclogitic Miscaschist Complex; EM – Emilius; GM – Gneiss Minuti complex; GP – Gran Paradiso; GR – Glacier-Rafray; IIDK – Seconda Zona Dioritico-Kinzigitica; MC – Mafic Complex; MM – Mont Mary; MR – Monte Rosa; PI – Pillonet; RCSZ – Roisan-Cignana Shear Zone; SA – Santanel; ST – Strona-Ceneri; VP – Valpelline series.

HT metamorphism in the host granulites (e.g., Ewing et al., 2013; Bartoli et al., 2024), the persistence of HT metamorphic conditions over time (e.g., Connop et al., 2024), and the timing and mechanism of deep crustal exhumation (e.g., Smye et al.2019; Wyatt et al., 2022).

Conflicting interpretations largely arise from the wide scatter in geochronological data across minerals and methods, with most ages ranging from 290 to 240 Ma (Guergouz et al., 2018; Langone et al., 2018; Kunz et al., 2018b; Wyatt et al., 2022; Bartoli et al., 2024; Connop et al., 2024). In Val Strona di Omegna, older ages occur in amphibolite-facies rocks farther from the Mafic Complex, while younger ages are found in granulite-facies rocks near the intrusive contacts. These younger dates are generally coeval with, or postdate, the emplacement of the Mafic Complex. Further ambiguity arises from contrasting interpretations of the contact between the Mafic Complex and the surrounding host rocks. Some studies report ultra-HT overprints and possible partial melting induced by the intrusion of the Mafic Complex (Ewing et al., 2013), whereas others describe lower-grade thermal aureoles that overprint earlier HT assemblages (e.g., Barboza and Bergantz, 2000).

Despite extensive research, geochronological constraints on the pre- to early Permian evolution of the deep Adriatic crust remain limited. Ages older than 290 Ma are particularly scarce in the Ivrea–Verbano zone, with only a few scattered late Carboniferous dates reported from zircon, monazite, and garnet (e.g., Ewing et al., 2013; Klötzli et al., 2014; Guergouz et al., 2018; Kunz et al., 2018b; Wyatt et al., 2022; Connop et al., 2024). Some authors suggest that substantial deep crustal exhumation may have occurred during this time, though the reliability of some of these older dates is debated due to limited reproducibility (Ewing et al., 2023).

The Valpelline series of the Dent Blanche nappe system (Fig. 1) exposes a continuous section of deep Adriatic crust. Notably, the area is free of Permian gabbros and exhibits only minor low-temperature Alpine overprinting, largely confined to localized shear zones (Kunz et al., 2018a; Caso et al., 2024a, and references therein). These features make Valpelline especially suitable for investigating Permian evolution, as they avoid the geochronological and metamorphic complexities associated with the Mafic Complex emplacement in the Ivrea–Verbano Zone.

2.2. *The Valpelline series*

The Valpelline series includes migmatitic gneiss and granulites that exceptionally preserve Permian HT mineral assemblages and structures (Fig. 2; Manzotti et al., 2018; Kunz et al., 2018a; Caso et al., 2024a). These rocks consistently exhibit three generations of HT foliations, with clear cross-cutting relationships and distinct mineral assemblages supporting each foliation (Table 1; Caso et al., 2024a; 2024b).

S1 is supported by granulite-facies minerals and occurs as a discordant internal foliation within mafic boudins hosted in migmatitic gneiss (Caso et al., 2024a; 2024b). These boudins are ubiquitously present in the Valpelline series, regardless of the mineral assemblage associated

Table 1
Summary of structures and metamorphic assemblages from the Valpelline series. Mineral abbreviations, here and elsewhere in the text, follow Whitney and Evans (2010).

	Migmatitic gneiss with mafic granulite boudins	
	Opx-bearing migmatite	Crd-bearing migmatite
S1	Opx + Pl + Amp ± Cpx ± Bt ± Grt ± Qz in mafic boudins	
S2	Bt + Grt + Opx + Pl + Qz ± Kfs ± Ilm (M1)	Bt + Grt + Crd + Pl + Qz + Ilm ± Sil (M2)
S3	Sil + Grt + Qz + Pl ± Bt + Ilm	

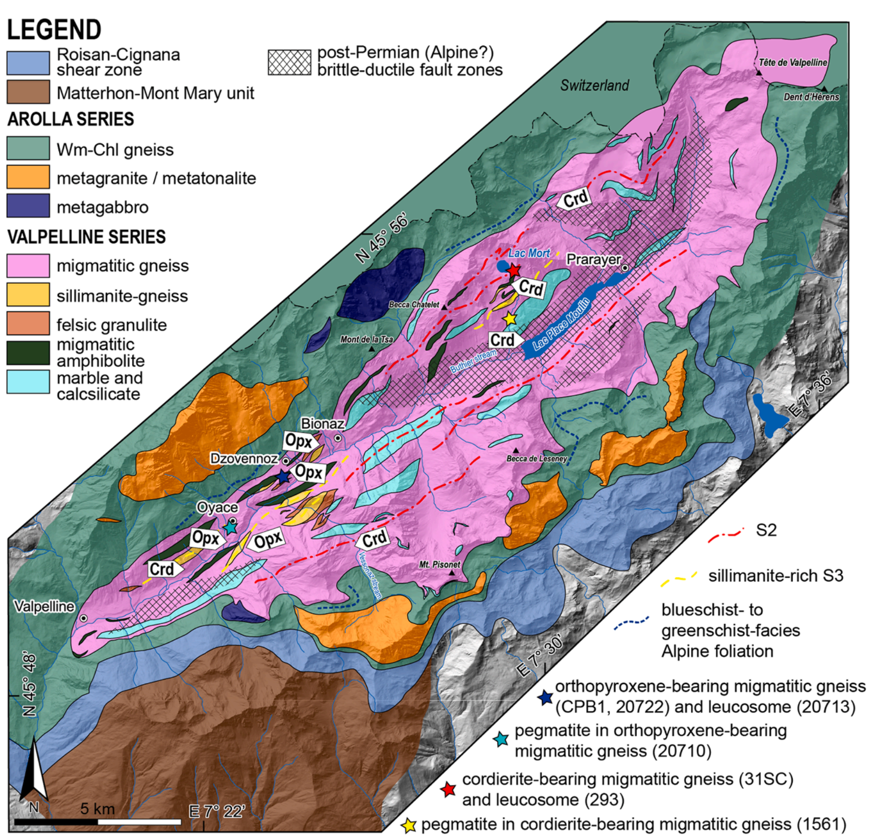

Fig. 2. Geological map of the Dent Blanche nappe system (modified after Caso et al., 2024a, and ref. therein; WGS84 geographic coordinates). The labels Opx and Crd indicate the main locations where orthopyroxene- and cordierite-bearing migmatitic gneiss are observed, respectively. Sampling locations for this study are marked with stars and labeled with sample names.

with external S2.

S2 is associated with extensive partial melting and is characterized by two distinct mineral assemblages in migmatitic gneiss, biotite–garnet–orthopyroxene (M1) and biotite–garnet–cordierite (M2). Ti-in-biotite geothermometry suggests that M1 developed at a higher temperature than M2 (Caso et al., 2024a). No overprinting relationships have been observed between these assemblages, although both are clearly bracketed in the relative structural chronology between S1 and S3 (Table 1; Caso et al., 2024a; 2024b).

Finally, S3 is related to pervasive folding of S2 and is characterized by retrograde sillimanite overgrowth in both Opx- and Crd-bearing migmatitic gneiss (Caso et al., 2024a; 2024b). A bimodal age

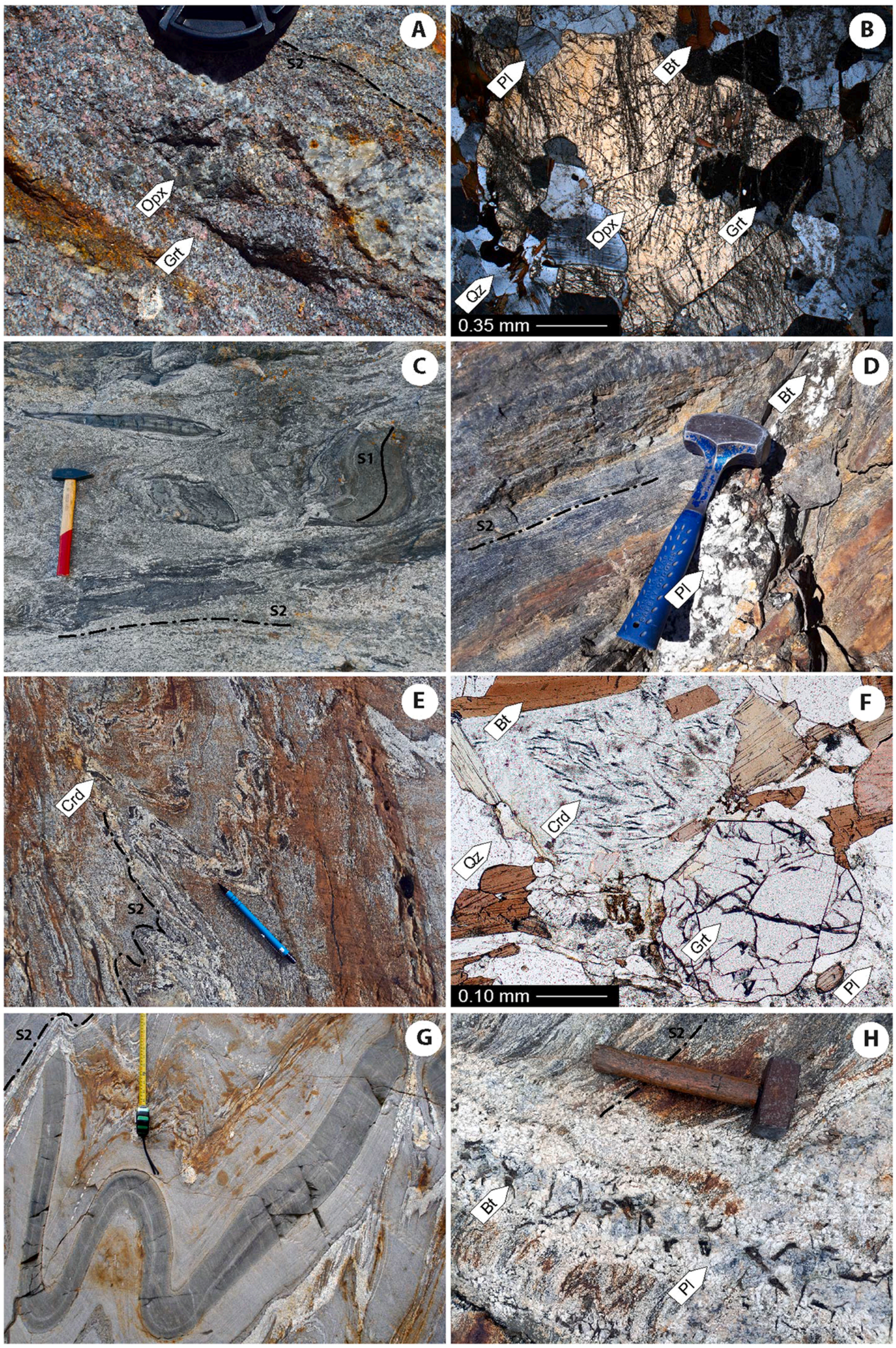

Fig. 3. Photographs and microphotographs of migmatitic gneiss and pegmatite from the Valpelline series at the sampling sites. A: Garnet and orthopyroxene assemblage in Opx-bearing migmatitic gneiss, Dzovennoz. B: Cross-polar microphotograph of Opx-bearing migmatite, Dzovennoz. C: Boudin of mafic granulite in orthopyroxene-bearing migmatitic gneiss, Oyace. D: Biotite-rich pegmatite in orthopyroxene-bearing migmatitic gneiss, Bionaz. E: Cordierite-rich leucosome in folded Crd-bearing migmatite, Lac Mort. F: Parallel-polar microphotograph of Crd-bearing migmatite, Lac Mort. G: Folded boudins of mafic granulite in Crd-bearing migmatitic gneiss, Lac Mort. H: Biotite-rich pegmatite in Crd-bearing migmatite, Lac Long. Labels: Bt – biotite, Crd – cordierite, Grt – garnet, Opx – orthopyroxene, Pl – Plagioclase, Qz – quartz.

distribution with partially resolved peaks at 283 ± 2 Ma and 266 ± 2 Ma has been already identified in sillimanite-rich migmatitic gneiss by LA-ICP-MS zircon dating, with Ti-in-zircon thermometry indicating crystallization temperatures below 750 °C (Kunz et al., 2018a).

3. Material and methods

3.1. Samples

In this study, samples of migmatitic gneiss and Bt-bearing pegmatite were collected in the Valpelline series (Fig. 2). Additional details on the sampling locations are provided in the Supplementary File.

Opx-bearing migmatitic gneiss (samples CPB1 and 21722) and leucosome (sample 20713) were collected at Dzovennoz (Fig. 2). The migmatitic gneiss consists of biotite, garnet, orthopyroxene, plagioclase, and quartz, with minor to rare K-feldspar and ilmenite. It exhibits S2 banding characterized by alternating layers of quartz–feldspar-rich leucosome and garnet–biotite-rich layers (Fig. 3A, 3B). The migmatitic gneiss is interlayered with migmatitic amphibolite containing amphibole, biotite, clinopyroxene, garnet, ilmenite, plagioclase, and quartz. Boudins of mafic granulite are common within the Opx-bearing migmatitic gneiss, enclosed within S2 and preserving an internal S1 (Fig. 3C). A sample of Bt-bearing pegmatite (20710) was collected at Oyace (Fig. 2) near the contact between migmatitic gneiss and amphibolite (Fig. 3D).

Crd-bearing migmatitic gneiss (sample 31SC) and leucosome (sample 293) were collected at Lac Mort (Fig. 2). The migmatitic gneiss consists of biotite, garnet, cordierite, plagioclase, quartz, ilmenite, and minor to rare sillimanite. Banding is defined by quartz–feldspar-rich leucosome and biotite–cordierite–garnet-rich layers (Fig. 3E, 3F). The alignment of cordierite and biotite grains defines the S2 foliation, which has been folded and locally overprinted by sillimanite-rich S3. Boudins of mafic granulite wrapped by S2 and preserving an internal S1 foliation are also common within the Crd-bearing migmatitic gneiss (Fig. 3G). A second sample of Bt-bearing pegmatite (sample 1561) was collected at Les Seytives, between Lac de Place Moulin and Lac Mort, where it intrudes the migmatitic gneiss (Fig. 3H).

3.2. Zircon separation and imaging

Samples 21722, 20713, 293, 20710, and 1561 were processed at the Earth Sciences Department (DISTAD) of the Università degli Studi di Milano to extract zircon crystals using standard mechanical, density, and magnetic separation techniques. Zircons were then mounted in epoxy resin, polished to expose the crystal interior domains and imaged by a JEOL JSM-IT 500 scanning electron microscope (SEM) equipped with a Deben-Centaurus cathodoluminescence detector.

3.3. Zircon trace element geochemistry

Zircon trace element analyses were performed at DISTAD by laser ablation-inductively coupled plasma mass spectrometry (LA-ICP-MS) using a Thermo-Scientific ICP-MS iCAP RQ single quadrupole interfaced to a 193 nm ArF excimer laser ablation system (Teledyne Analite Excite) equipped with a HelEx 2 vol sample chamber. We set an ablation spot of 25 μm in diameter, a repetition rate of 10 Hz, and a fluence of 2 J/cm^2. Each analysis comprised 40 s of background acquisition and 60 s of ablation signal. Dwell times were 5 ms for ^{29}Si and ^{90}Zr, 100 ms for Ti and 30 ms for the other analytes. For concentration calculations, average background-subtracted count rates were internally normalized to ^{29}Si, using the stoichiometric SiO_2 content of 32.78 wt % in zircon. Additional information on method and data treatment is reported in the Supplementary File. Data are reported in Table S1.

3.4. LA-ICP-MS U-Pb zircon dating

In-situ U–Pb zircon dating was carried out during two analytical sessions using the same instrumentation and set up described for trace element analysis. The masses 202, 204, 206, 207, 208, 232, and 238 were measured using a dwell time of 10 ms and a spot size of 20 μm in diameter. Laser-induced elemental fractionation and instrumental mass bias were corrected by normalization to the 91500 zircon reference (1065 Ma, Wiedenbeck et al., 2004). The analytical uncertainties of individual spot analyses were propagated by quadratic addition of the excess scatter, which was calculated from reference material analyses following Horstwood et al. (2016). Additional information on method and data treatment is provided in the Supplementary File. Data are reported in Table S2.

3.5. CA-ID-TIMS U-Pb zircon dating

High-precision U–Pb zircon dating was undertaken at the University of Geneva by chemical abrasion of individual zircons grains (Mattinson, 2005), involving annealing in a muffle furnace at 900 °C for 48 h and chemical abrasion for 12 h at 210 °C in concentrated HF. The chemically abraded grains were then loaded for dissolution into 200 μl Savillex microcapsules with ∼ 5 mg of EARTHTIME ^{202}Pb–^{205}Pb–^{233}U–^{235}U tracer solution (Condon et al. 2015) and put into an oven at 210 °C for 48 h.

The isotopic analyses were performed at University of Geneva on a TRITON mass spectrometer equipped with a MasCom discrete dynode electron multiplier. Lead isotopic fractionation was corrected based on the certified value of ^{202}Pb/^{205}Pb = 0.99924 ± 0.03 %, 1σ of the tracer. The U mass fractionation for the same analyses was calculated using the ^{233}U-^{235}U ratio of the double spike solution (0.99506 ± 0.01 %, 1σ). Lead isotope compositions were measured on the electron multiplier, while U (as UO_2) isotopic measurements were made in static Faraday mode (using amplifiers equipped with 10^{13}Ωresistors) or, in case of insufficient U beam size, on the electron multiplier.

The initial statistics, data reduction, and age calculation were done using the TRIPOLI and Redux software (Bowring et al., 2011). All ^{206}Pb/^{238}U and ^{207}Pb/^{206}Pb ratios were corrected for initial disequilibrium in ^{230}Th/^{238}U using Th/U [magma] = 3.5 ± 1 (1σ). Additional information for the method is provided in Supplementary File, while all data are reported in Table S3.

3.6. Phase assemblage modeling and Ti-in-zircon thermometry

Phase assemblage modeling was carried out in the CaO-Na_2O-K_2O-FeO-MgO-Al_2O_3-SiO_2-H_2O-TiO_2 (CNKFMASHT) chemical system using the GeoPS software (Xiang and Connolly, 2022), along with the DS62 thermodynamic dataset (Holland and Powell, 2011) and activity-composition (a-x) models for high-temperature metapelites (White et al., 2014). The full list of a–x models used is provided in the Supplementary File. The uncertainties in determining P-T conditions by phase assemblage modeling are lower than ± 0.1 GPa and ± 50 °C at the 2σ level and are considered equivalent to the size of the P-T field of interest, making it the most powerful tool for P-T estimates (Powell and Holland, 2008).

Ti-in-zircon temperature was calculated using the pressure-dependent equation from Crisp et al. (2023). This calibration is associated with a total uncertainty of ± 40 °C, while the analytical error for Ti (1σ) was <1 ppm, corresponding to an uncertainty of about ± 10 °C. The activities of SiO_2 and TiO_2 have been set to 0.90 and 0.45, respectively. These values in agreement with values considered for ilmenite-bearing rocks (Crisp et al., 2023 and ref. therein) and consistent with those calculated by phase modeling. The results are reported in Table S3.

4. Results

4.1. Zircon morphology

Zircon grains exhibit significant textural variability, with minor differences observed between migmatitic gneiss, leucosomes, and pegmatites. The full documentation of zircon cathodoluminescence images is provided in Fig. S1.

In the Opx-bearing migmatitic gneiss (sample 21722, Fig. 4a–c), zircon grains have either elongated or stubby habits and often host partially resorbed xenocrystic cores. These inherited cores are generally bright in CL and display relict internal zoning truncated by external overgrowths. Surrounding the xenocrystic core, thin (<10 μm) irregular rings with bright homogeneous emission are commonly observed and interpreted as zones formed through dissolution-precipitation. Further out, overgrowths of variable thickness show sector zoning and planar growth zoning, with occasional internal resorption surfaces. Thin, dark and uniform outer rims are occasionally present.

In the leucosome of the Opx-bearing migmatitic gneiss (sample 20713), zircon grains are elongated or stubby and xenocrystic cores are rare (Fig. 4d–f). These grains are characterized by concentric oscillatory zoning and sector zoning. Many grains exhibit faintly zoned centers surrounded by fine-scale oscillatory zoned rims. These domains are usually separated by resorption surfaces. Similar zircon characteristics are found in the pegmatite intruding into Opx-bearing migmatitic gneiss (sample 20710), where xenocrystic cores are absent (*Fig. 4g*–i). Rounded "soccerball-shaped" zircons with multiple crystal facets are more rarely present.

Most of the zircon grains in the leucosome of the Crd-bearing migmatitic gneiss (sample 293, Fig. 4j–l) display small xenocrystic cores, which can appear either bright or dark in CL. These cores exhibit internal zoning truncated by external overgrowths and are surrounded by thin dissolution-precipitation rings. The external overgrowths mostly show sector zoning and multiple crystal facets are observed. Zircon grains in the pegmatite intruding into the Crd-bearing migmatitic gneiss (sample 1561) are mostly dark in CL and display core-to-rim fine scale oscillatory zoning. These grains do not show xenocrystic cores (Fig. 4n–q).

4.2. U-Pb zircon dating

4.2.1. LA-ICP-MS zircon dating

LA-ICP-MS U-Pb zircon dating was conducted on texturally heterogeneous zircon grains from migmatitic gneiss and pegmatites. $^{206}Pb/^{238}U$ weighted mean age plots are shown in Fig. 5. Additional data representation is provided in the Supplementary File.

Twenty spot analyses were performed on zircon grains from the Opx-bearing migmatitic gneiss (sample 21722). Seven analyses of xenocrystic cores previously identified using CL images plot along the concordia line between 488 and 653 Ma (see Supplementary File). The other twelve dates yield a $^{206}Pb/^{238}U$ weighted mean age of 291.4 ± 1.6 Ma (MSWD = 2.2; Fig. 5A). In addition, nineteen spot analyses were performed on zircon grains separated from the leucosome of the Opx-bearing migmatitic gneiss (sample 20713) and yield a $^{206}Pb/^{238}U$ weighted mean age of 294.4 ± 1.1 Ma (MSWD = 4.3; Fig. 5B). Finally, twenty-one spot analyses on the pegmatite sample 20710 yield a $^{206}Pb/^{238}U$ weighted mean age of 294.1 ± 1.0 Ma (MSWD = 3.5; Fig. 5C). The ages obtained for the Opx-bearing migmatitc gneiss and the releted pegmatite are indistinguishable within analytical uncertainty.

Furthermore, twenty-four spot analyses were performed on zircon crystals from the leucosome of the Crd-bearing migmatitic gneiss (sample 293). Five analyses on xenocrystic cores gave concordant to subconcordant apparent $^{206}Pb/^{238}U$ ages ranging from 511 to 726 Ma (see Supplementary File). The other nineteen dates yield a $^{206}Pb/^{238}U$ weighted mean age of 286.8 ± 1.1 Ma (MSWD = 1.7; Fig. 5D). In addition, nineteen spot ages from zircon grains separated from pegmatite sample 1561 yield an undistinguishable $^{206}Pb/^{238}U$ weighted mean age of 287.2 ± 1.2 Ma (MSWD = 1.8; Fig. 5E). The results consistently show that the Crd-bearing leucosome and related pegmatite are younger than the Opx-bearing migmatitic gneiss.

4.2.2. CA-ID-TIMS zircon dating

CA-ID-TIMS zircon dating was performed on twenty-six crystals from three samples previously investigated by LA-ICP-MS. All crystals were imaged by CL and we selected only those that do not show any discernible inherited cores. Moreover, we selected crystals showing a range of zircon sizes, morphologies, and internal textures.

Eight crystals were analyzed from the leucosome of Opx-bearing migmatitic gneiss (sample 20713, Fig. 5F), yielding scatter in $^{206}Pb/^{238}U$ dates from 289.72 ± 0.19 to 295.25 ± 0.15 Ma. Among the six oldest concordant analysis, three are showing undisturbed, simple oscilatory zone pattern, overlapping within the uncertainty and yielding weighted mean $^{206}Pb/^{238}U$ date of 294.29 ± 0.38 Ma (MSWD = 3.5). The remaining three older grains scatter along the concordia likely due to inheritance, which may be evidenced in CL images as truncated oscillatory zoning in grains z13a and z16a, and resorption with overgrowth in grain z8a, or possibly due to inherited cores that are not visible in the analyzed grains but are present in other grains (Supplementary File). The youngest two grains are showing thin white rim in grain z1a or internal white areas in grain z10a in CL images

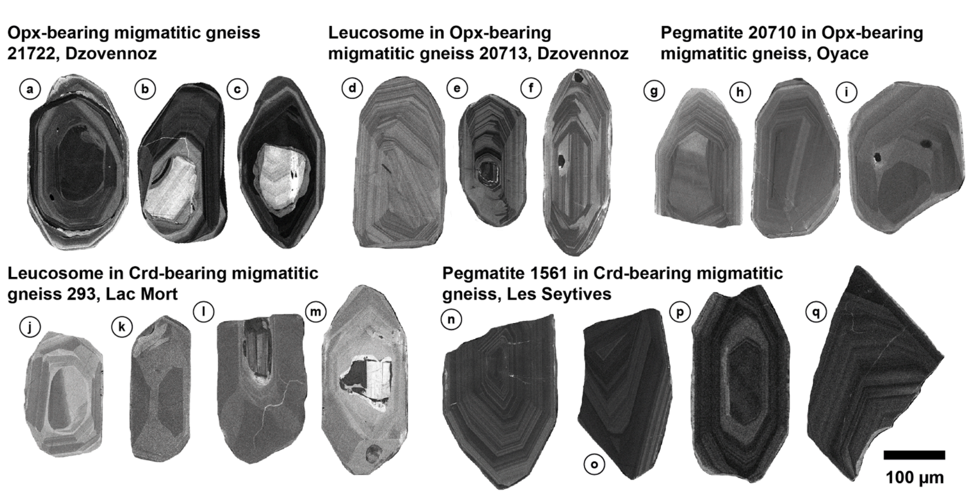

Fig. 4. Cathodoluminescence imaging of selected zircon grains (a-q) divided by rock-type and sampling locality (cfr. Fig. 2). Further images are in the Supplementary File.

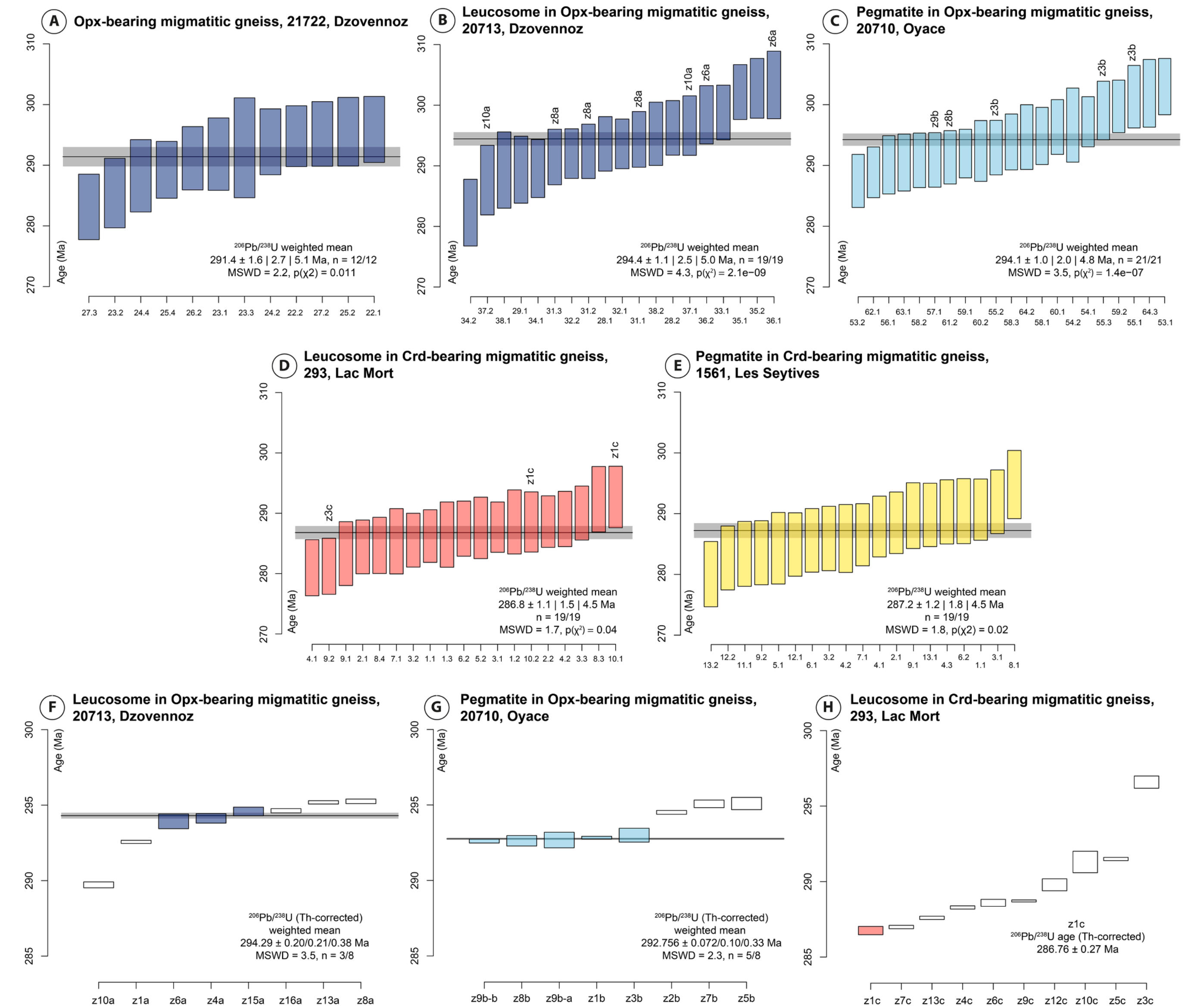

Fig. 5. $^{206}Pb/^{238}U$ dates of zircons analyzed by LA-ICP-MS (A–E) and CA-ID-TIMS (F–H). Additional details on sampling locations, selected grains, analytical spots, and results are provided in Fig. 2 and Supplementary File. Colored boxes indicate the analytical spots used to calculate the $^{206}Pb/^{238}U$ weighted mean ages or considered as individual ages. In A – E diagrams, the $^{206}Pb/^{238}U$ weighted mean ages are reported at 2σ confidence level using the notation age ± α|β|γ, where α represents the analytical uncertainty, β includes an additional overdispersion term following Vermeesch, 2018, and γ further propagates the systematic uncertainties (cfr. Horstwood et al., 2016). Xenocrystic cores were excluded from the $^{206}Pb/^{238}U$ weighted mean age calculations. In F – H diagram, the $^{206}Pb/^{238}U$ weighted means are reported at 2σ confidence level using the notation age ± x|y|z, where x is the internal error in absence of all systematic errors, y includes the tracer calibration error, and z includes both tracer calibration and decay constant errors (cfr. Schoene et al., 2006).

(Supplementary File), which may be result of fluid flow and, possibly, a reason for unresolved lead loss.

Eight zircon grains were analyzed from the pegmatite that intrudes into the Opx-bearing migmatitic gneiss (sample 20710; Fig. 5G). Five concordant analyses yield overlapping $^{206}Pb/^{238}U$ dates within analytical uncertainty, defining a weighted mean age of 292.76 ± 0.33 Ma (MSWD = 2.3). The remaining three crystals are older, with individual $^{206}Pb/^{238}U$ dates ranging from 294.51 ± 0.13 to 295.10 ± 0.41 Ma. When pooled, these three older analyses yield a weighted mean age of 294.66 ± 0.22 Ma (MSWD = 2.6). One of them (z7b, see Supplementary File) displays a distinctive "soccerball-shaped" morphology.

Lastly, ten crystals were analyzed from the leucosome of the Crd-bearing migmatitic gneiss (sample 293; Fig. 5H). Two of them are discordant and yielded $^{206}Pb/^{238}U$ dates older than 291 Ma (Supplementary File). The remaining eight analysis are scaterring along the concordia with $^{206}Pb/^{238}U$ dates varying from 286.76 ± 0.27 to 291.49 ± 0.11 Ma (Fig. 5H).

4.3. Trace element geochemistry of zircon

Zircon grains in the leucosome of the Opx-bearing migmatitc gneiss (sample 20713) share relatively flat HREE patterns with $Lu_N/Sm_N = 2–8$ (the subscript N indicates chondrite normalization; Fig. 6A). These grains have similar negative Eu anomalies (Eu/Eu* = 0.2; Fig. 6B), high Th/U (0.3–0.6; Fig. 6C), and variable Ti contents (6–20 ppm; Fig. 6D), with an average Ti content of 11 ppm. In the leucosome of the Crd-bearing migmatitic gneiss (sample 293), zircon grains show steep positive HREE patterns with Lu_N/Sm_N of 64–112 (Fig. 6A). These crystals share strong negative Eu anomalies (Eu/Eu* = 0.1; Fig. 6B), as well as relatively low Th/U (<0.1; Fig. 6C) and Ti contents (4–6 ppm; Fig. 6D).

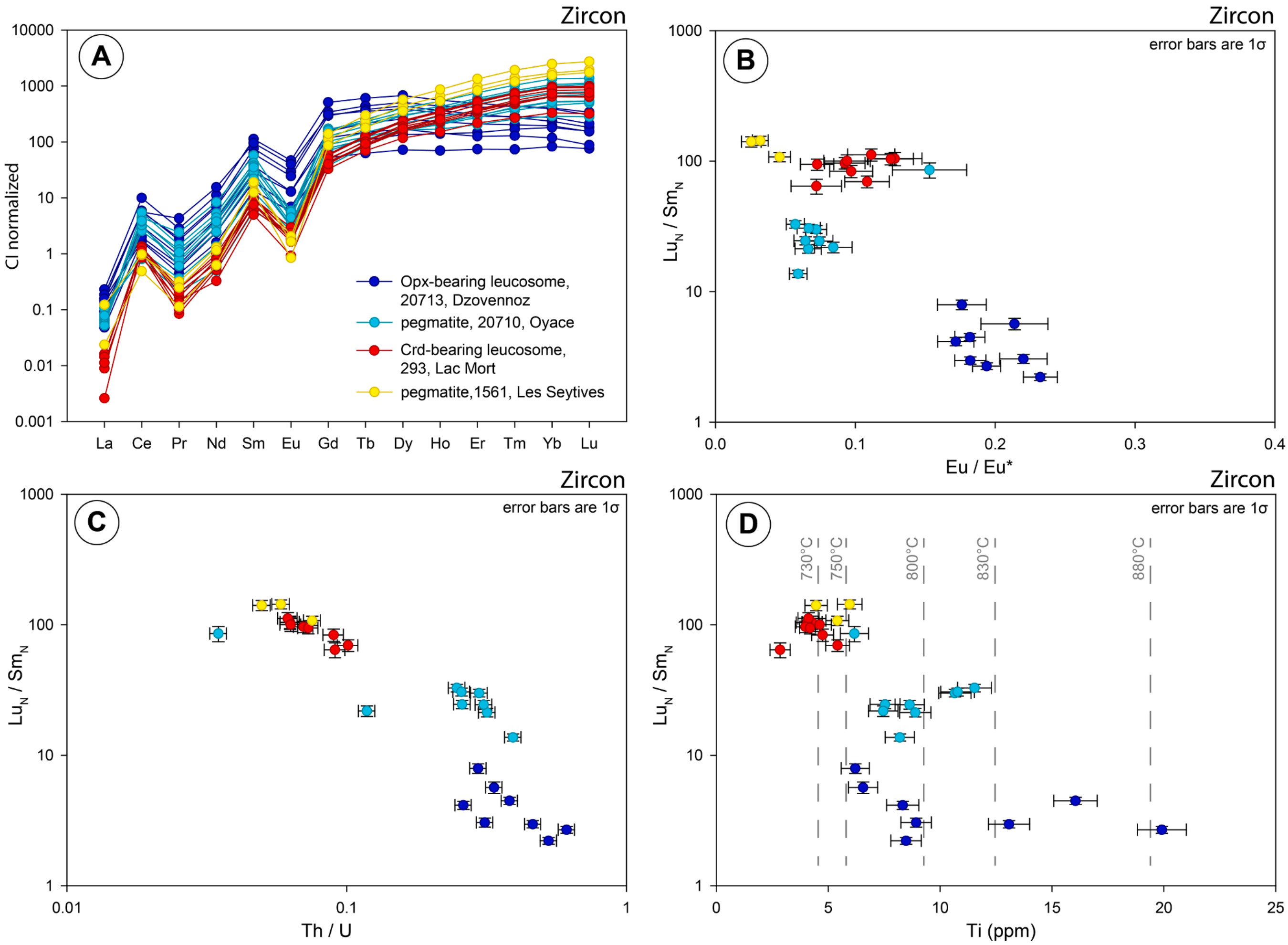

Fig. 6. Trace and rare earth element concentrations for zircon crystals from leucosomes and pegmatites of the Valpelline Series. Where indicated, data are normalized to the chondrite values of Taylor and McLennan, 1995. Colors refer to different lithotypes and locations and are consistent across all plots. Error bars are 1 σ. A: Zircon normalized rare earth element patterns. B: Plot of Lu_N/Sm_N versus Eu/Eu*. C: Plot of Lu_N/Sm_N versus Th/U. D: Plot of Lu_N/Sm_N versus Ti. Ti-in-zircon temperature is calculated following the calibration by Crisp et al. (2023).

Zircon grains in the pegmatite sample 20710 show moderately steep HREE patterns (Lu_N/Sm_N = 14–86; Fig. 6A), pronounced negative Eu anomalies (Eu/Eu* = 0.1–0.2; Fig. 6B), variable Th/U ratios (0.1–0.4; Fig. 6C), and Ti contents from 6 to 12 ppm (Fig. 6D). These crystals have higher Lu_N/Sm_N and lower Eu/Eu* than those in the host Opx-bearing migmatitic gneiss. Finally, zircon grains in the pegmatite sample 1561 show steep HREE patterns (Lu_N/Sm_N = 108–144; Fig. 6A), strong negative Eu anomalies (Eu/Eu* <0.1; Fig. 6B), low Th/U ratios (<0.1; Fig. 6C) and modest Ti contents (4–6 ppm; Fig. 6D). In this pegmatite, zircon grains exhibit steeper HREE patterns and more pronounced Eu/Eu* anomalies than in the host Crd-bearing migmatitic gneiss, while maintaining similar Th/U ratios and Ti contents.

4.4. Metamorphic P-T conditions

4.4.1. Phase assemblage modeling and Ti-In-zircon thermometry

The first P–T pseudosection (Fig. 7A) models the M1 mineral assemblage (Bt + Grt + Opx + Pl + Qz ± Kfs ± Ilm, Table 1) in the Opx-bearing migmatitic gneiss (sample CPB1) with a bulk composition of SiO_2 = 56.96 wt%, Al_2O_3 = 16.42 wt%, FeO = 10.37 wt%, MgO = 4.63 wt%, TiO_2 = 0.54 wt%, CaO = 3.73 wt%, Na_2O = 2.77 wt%, K_2O = 3.66 wt%. An H_2O content corresponding to LOI (0.90 wt%) is assumed. The pseudosection incorporates isopleths for the garnet end-members almandine and pyrope, covering the garnet composition range ($Alm_{59–65}$, $Py_{23–28}$, $Grs_{8–11}$, Supplementary File). The stability fields for this garnet include conditions with mineral assemblages such as Bt + Grt + Opx + Pl + Qz + Kfs + Melt, Bt + Grt + Ilm + Opx + Pl + Qz + Kfs + Melt, and Bt + Grt + Ilm + Opx + Pl + Kfs + Melt, all aligning with the mineral assemblage observed in the sample and considering potential uncertainties about the role of quartz, whether as part of the assemblage or crystallized from the melt. The predicted metamorphic conditions for the M1 assemblage are approximately 0.8–1.0 GPa and 870–890 °C.

The second pseudosection (Fig. 7B) models the M2 mineral assemblage (Bt + Grt + Crd + Pl + Qz ± Sil, Table 1) in the Crd-bearing migmatitic gneiss (sample 31SC), with a bulk composition of SiO_2 = 55.86 wt%, Al_2O_3 = 18.95 wt%, FeO = 8.33 wt%, MgO = 4.17 wt%, TiO_2 = 1.08 wt%, CaO = 1.74 wt%, Na_2O = 2.85 wt%, K_2O = 2.67 wt%. An H_2O content of 1.36 wt% is assumed, slightly below the LOI value of 2.20 wt%. This pseudosection includes end-member isopleths for garnet ($Alm_{70–74}$, $Py_{23–26}$, $Grs_{2–3}$, Supplementary File), encompassing the garnet composition identified in mineral analyses. The stability fields for this assemblage include conditions with or without sillimanite and K-feldspar, reflecting small P–T variations. The predicted equilibrium metamorphic conditions for the Crd-bearing migmatitic gneiss are around 0.4–0.6 GPa and 680–760 °C, which are lower than those for the Opx-bearing migmatitic gneiss.

Finally, Ti-in-zircon thermometer is applied to zircon grains in leucosome and pegmatite to obtain an independent estimate of the crystallization temperature (Fig. 6). The temperature calculated for the leucosome of the Opx-bearing migmatitic gneiss (sample 20713) ranges

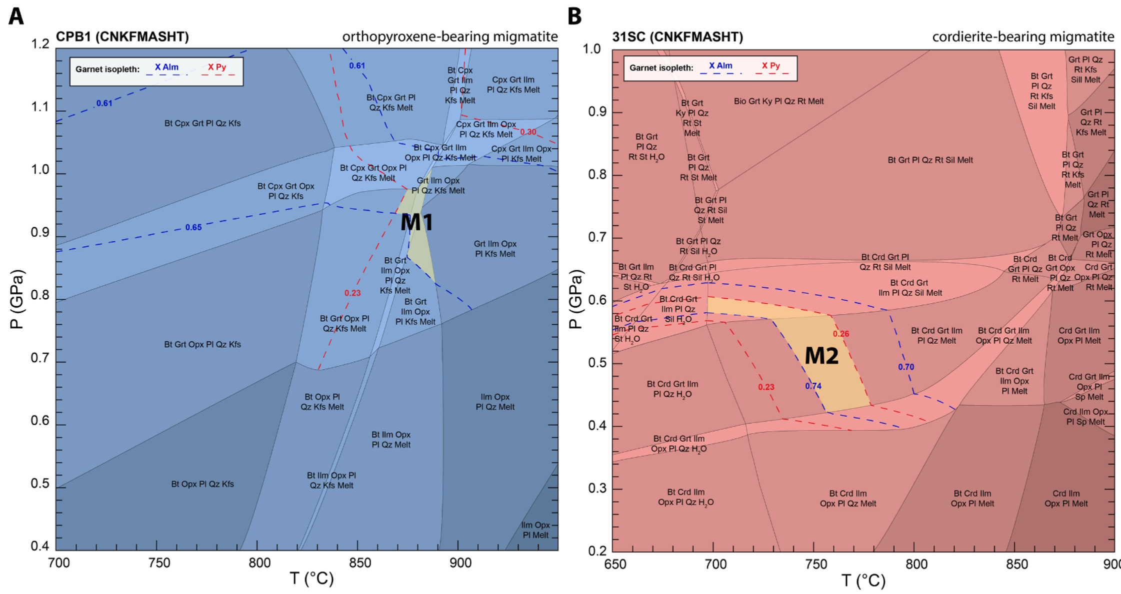

Fig. 7. P-T pseudosections exploring the stability conditions of Opx-bearing (M1) and Crd-bearing (M2) assemblages in the migmatites of the Valpelline series (A and B, respectively). Garnet almandine and pyrope isopleths are reported in blue and red, respectively (see also the Supplementary File). The P-T fields of interest are contoured yellow.

from 760 °C to 890 °C at a pressure of 0.9 GPa, with a median value of 797 °C and an interquartile range of 72 °C. For the pegmatite sample 20710, temperature is between 760 °C and 830 °C, with a similar median value. Conversely, zircon from the leucosome of the Crd-bearing migmatitic gneiss (sample 293) yields a temperature between 682 °C and 739 °C at a pressure of 0.5 GPa, with a median of 715 °C and a narrow interquartile range of 5 °C. These temperature estimates are similar to those derived for the pegmatite sample 1561, which range from 721 °C to 748 °C.

5. Discussion

5.1. Zircon dating

The LA-ICP-MS U–Pb zircon dates suggest an age distinction between the two types of migmatitic gneiss (Fig. 5). For instance, there is a difference of approximately 7–8 million years between the $^{206}Pb/^{238}U$ weighted mean age of the leucosome of the Opx-bearing migmatitic gneiss (sample 20713, 294.4 ± 2.5 Ma) and that of the Crd-bearing migmatitic gneiss (sample 293, 286.8 ± 1.5 Ma). A similar age difference is also observed between the two pegmatites intruded into the respective migmatitic gneiss types (Fig. 5), further supporting the interpretation of two temporally distinct crystallization events.

However, when the propagation of systematic uncertainties is taken into account, which is necessary to extrapolate the results beyond a single analytical session, the two age populations partially overlap (Fig. 5). The difference between the two events approaches the 1.5–2 % uncertainty threshold, which cannot be resolved using LA-ICP-MS techniques (Schaltegger et al., 2015; Horstwood et al., 2016). This level of uncertainty limits meaningful comparison with the regional geological history and, more importantly, prevents a reliable estimate of the time interval required to calculate the average exhumation rate. These limitations are addressed by CA-ID-TIMS U–Pb zircon dating, which provides significantly higher precision and accuracy (both better than 0.1 %; e.g., Condon et al., 2024). However, because this method involves dissolving entire zircon grains, it has required careful textural driven interpretation.

The CA-ID-TIMS U–Pb zircon dates from the leucosome of the Opx-bearing migmatitic gneiss (sample 20713) show a certain degree of scatter (Fig. 5f), which is interpreted, with reference to the older grains, as resulting from inheritance, often evidenced by the presence of xenocrystic cores in a few discarded grains. As for the anomalously younger dates, these may reflect incomplete removal of lead loss during chemical abrasion, a phenomenon also observed in other CA-ID-TIMS studies reporting anomalously young ages (e.g., Schoene et al., 2010; Gaynor et al., 2022), or compositional zoning of zircons caused by successive metamorphic crystallization events, as indicated by the thin outer rims. The most reliable estimate for zircon crystallization is thus given by the weighted mean of grains z6a, z4a, and z15a, which are texturally more suitable for this technique (294.29 ± 0.38 Ma; Fig. 5f).

The interpretation of the dates from the pegmatite sample 20710 is more uncertain. We consider the age of five zircon crystals yielding a $^{206}Pb/^{238}U$ weighted mean age of 292.76 ± 0.33 Ma (*Fig. 5g*) to most likely represent the emplacement age of the pegmatite in the Opx-bearing migmatitic gneiss. We do not consider the possible weighted mean of 294.66 ± 0.22 Ma calculated from the three oldest grains because they are slightly discordant and may therefore contain inheritance from the host rock, although this result does not affect any of the interpretations.

Zircon crystals from the leucosome of the Crd-bearing migmatitic gneiss (sample 293) show a significant age span. Even after excluding the two oldest, highly discordant grains, the remaining dates range between 286.76 ± 0.27 Ma and 291.49 ± 0.11 Ma along the Concordia line, without forming clear age clusters (Fig. 5H). Notably, the concordant results are consistently younger than those obtained from the Opx-bearing migmatitic gneiss.

Cathodoluminescence (CL) images (Fig. 3) reveal that the zircon grains from this sample often contain significant volumes of inherited cores. Although grains without obvious old cores were selected, it is impossible to exclude the presence of tiny, undetected xenocrystic cores within the analyzed crystals. Therefore, we propose that the simplest explanation for the age dispersion is cryptic inheritance: the oldest concordant zircon age (291.49 ± 0.11 Ma) likely reflects a mixture between the younger zircon population and a minor (<2 %) contribution from a ca. 500 Ma xenocrystic core (see Supplementary File). Conversely, the two youngest analyses for sample 293 overlap within their uncertainty ranges. Therefore, it is suggested that the best estimate for the crystallization age of the leucosome of the Crd-bearing migmatitic gneiss is the youngest zircon age of 286.76 ± 0.27 Ma, confirming the results obtained in-situ via LA-ICP-MS. This indicates that the leucosome in the Crd-bearing migmatitic gneiss is 7.53 ± 0.47 million years younger than the leucosome in the Opx-bearing migmatitic gneiss.

5.2. Metamorphic evolution

Phase assemblage modeling reveals the occurrence of two distinct metamorphic events in the migmatitic gneiss of the Valpelline series. The first event, recorded by the Opx-bearing assemblage M1, took place under deep-crustal P-T conditions ($P = 0.8$–1.0 GPa and $T = 870$–890 °C) at 294.29 ± 0.38 Ma. M1 was followed by a second metamorphic event, marked by the Crd-bearing assemblages M2, which developed at 286.76 ± 0.27 Ma under mid-crustal P-T conditions ($P = 0.4$–0.6 GPa and $T = 680$–760 °C).

The M1 to M2 metamorphic evolution recorded in the migmatitic gneiss of the Valpelline series is associated not only with cooling and exhumation from the deep to the middle crust, but also with a significant change in the thermal gradient. Considering an average crustal density of 2800 kg/m^3, the thermal gradient rises from approximately 27 ± 3 °C/km during M1 to about 40 ± 8 °C/km during M2. The former gradient may reflect either collisional or post-collisional thermal relaxation, a phase of thermal disturbance, or a transition between the two (England and Thompson, 1984). In contrast, M2 reflects a more pronounced thermal anomaly.

We speculate that M1 represents a transitional phase, possibly connected to the late Variscan evolution within the Adriatic domain, although both metamorphic and geochronological evidence of this Variscan evolution are limited, as also observed in other parts of the deep Adriatic crust (e.g., Ewing et al., 2023). The thermal gradient characterizing M2 is best explained by a setting dominated by extension at the plate margins, which induces asthenosphere upwelling (e.g. Roda et al., 2019). Notably, despite the extensive exposure of the Adriatic basement in the Valpelline series, there is no evidence for gabbro intrusion. This absence supports our interpretation that the M2 metamorphic conditions resulted from a regional thermal regime rather than a local anomaly caused by mafic magma underplating, although the latter cannot be completely ruled out.

The chemical composition of zircon independently supports the temperature estimates for M1 and M2. Zircon crystals in the leucosome of the Opx-bearing migmatitic gneiss (sample 20713) have the lowest HREE concentrations, associated to the highest Ti contents and Th/U ratios (Fig. 6). Taken together, these data suggest crystallization at high temperature (> 800 °C), in the presence of garnet and possibly under conditions where monazite is scarce (cfr. Hermann and Rubatto, 2003). In contrast, zircon crystals in the leucosome of the Crd-bearing migmatitic gneiss (sample 293) have steeper HREE profiles, low Th/U ratios and Ti contents (Fig. 6). These characteristics suggest that these zircons crystallized at a lower temperature (710–720 °C) than those in the Opx-bearing migmatitic gneiss, with a lesser amount of garnet present in the stable assemblage and within the monazite stability field.

Zircon grains from the Valpelline series display a compositional evolution over time that differs from the patterns observed in other regions of the Adriatic basement. In particular, in other areas, such compositional changes are often attributed to contact metamorphism or fluid release caused by gabbro emplacement, or to the prolonged persistence of HT metamorphic conditions (e.g. Kunz et al., 2018b; Ewing et al., 2013; 2023).

5.3. Permian evolution of the Adriatic basement

The Valpelline Series enabled the reconstruction of a two-stage exhumation P–T–t path (Fig. 8), effectively avoiding the complicating effects of localized thermal disturbances associated with gabbro

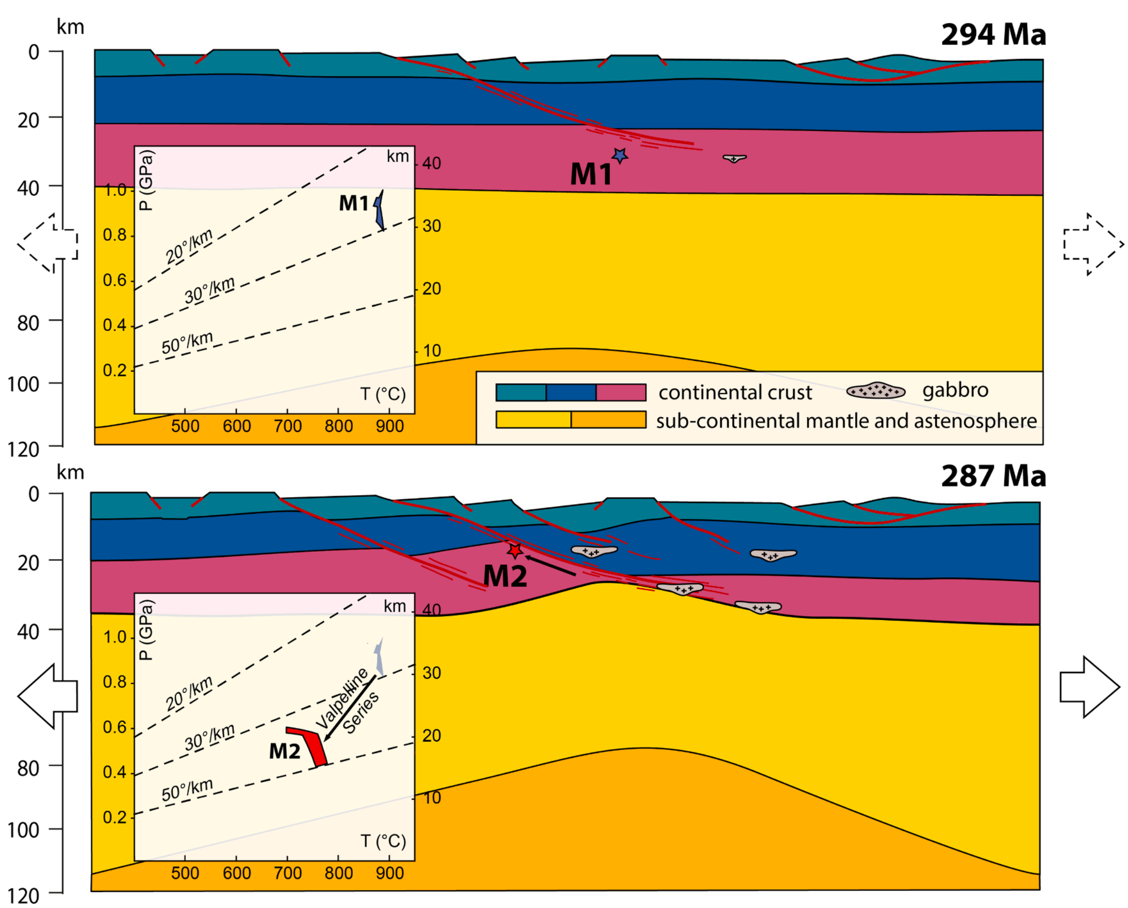

Fig. 8. Conceptual diagram of the evolution of the Adriatic crust between 294 and 287 Ma and summary of the P-T-t evolution of the Valpelline series.

emplacement and fluid circulation, which are commonly reported in other sectors of the Adriatic basement, including the Ivrea–Verbano zone (e.g., Vavra and Schaltegger, 1999; Ewing et al., 2013; Bartoli et al., 2024). This study demonstrates that the most of exhumation in the Valpelline series took place during the early Permian, before 286.76 ± 0.27 Ma, involving a shift from deep to mid-crustal levels alongside an increase in thermal conditions. Exhumation and cooling likely preceded the emplacement of Permian gabbro in the central and western Alps at 282–290 Ma (Petri et al., 2017; Roda et al., 2019; Karakas et al., 2019). This timing broadly coincides with the development of M2 metamorphic conditions in the Valpelline series and represents the peak thermal gradient conditions.

A P–T–t path similar to that identified in the Valpelline series has already been tentatively suggested in other regions of the Adriatic basement. In particular, in the Ivrea–Verbano zone, recent monazite petrochronology suggest that most deep crust exhumation occurred between approximately 310 Ma and the emplacement of the Mafic Complex at 282–286 Ma (Wyatt et al., 2022). However, available data older than 290 Ma are limited, making it challenging to draw definitive conclusions about early Permian events. Additionally, factors such as decoupling of zircon U-Pb ages from compositional changes at HT conditions (Kunz et al., 2018b) and fluid-induced Pb loss (Vavra and Schaltegger, 1999) have likely impeded preservation or detection of the early Permian record. In the central Alps, early Permian exhumation is also recorded within the Languard-Campo nappe; however, most of this exhumation postdates the emplacement of the Sondalo gabbro (286–289 Ma), and the precise timing of its metamorphic evolution remains poorly constrained due to the lack of geochronological data for the early stages (Petri et al., 2017; Roda et al., 2018).

The exhumation rate in the Valpelline series is estimated at 2.0 ± 1.0 mm/year, calculated over a relatively brief period of less than 8 million years. Kunz et al. (2018a) reported younger LA-ICP-MS zircon ages in sillimanite-rich rocks (283 – 266 Ma) and Ti-in-zircon temperature down to 630 °C, suggesting that cooling and possibly exhumation of the Valpelline series may have continued during the development of sillimanite-rich S3 (Caso et al., 2024b). Subsequently, the Valpelline series may have reached upper crust levels, experiencing low-grade conditions that are difficult to resolve with current techniques. However, sustaining such an exhumation rate over a longer period would be geologically unrealistic, as it would likely have led to continental breakup within 15–20 million years. This contrasts with the earliest evidence of oceanization in the Alps, which dates back to the Jurassic (Roda et al., 2019 and references therein).

The P–T–t path of the Valpelline series suggest that, during the early Permian, the lithosphere was subjected to a tectonic regime marked by episodic and high-velocity events. The potential spatial migration of the exhumation domain is also noteworthy. Boscaini et al. (2025) document a Permian magmatic rejuvenation migrating eastward across the Alps, which is interpreted as reflecting the direction of deep crustal delamination. This eastward migration correlates with the ages up to 294 Ma determined in the migmatitic gneiss of the Valpelline series in the western Alps, representing some of the oldest ages currently documented within the Adriatic basement.

Finally, some authors interpret the scatter observed in geochronological data from different phases in the Adriatic basement and in particular in the Ivrea–Verbano zone as evidence for the persistence of HT metamorphic conditions, possibly throughout the entire Permian (e.g., Guergouz et al., 2018; Wyatt et al., 2022; Connop et al., 2024). Similar scenarios are documented in many high-grade Cambrian-Ordovician (e.g., Northern Sierra de Quilmes in Argentina, Wolfram et al., 2019) and Proterozoic terrains (e.g., Central Domain of the Araçuai belt in Brazil, Cavalcante et al., 2018; Aus terrain in Namibia, Diener et al., 2013; Reynolds range, Rubatto et al., 2001). The Valpelline Series differs from the Ivrea–Verbano Zone in two main aspects. First, no significant age scatter is observed as our result are constarined to a much narroweer time interval of approximately 7–8 million years. Second, a cooling of approximately 100 ..C between M1 and M2 is recorded, making it unlikely that HT conditions persisted for an extended period. It is also worth noting that in the Ivrea–Verbano Zone, the youngest ages correspond to the highest temperature and pressure conditions, whereas in the Valpelline Series these conditions are associated with the oldest ages (M1).

6. Conclusion

The application of U-Pb zircon dating on the migmatitic gneiss of the Valpelline series has allowed us to constrain the timing of its early Permian metamorphic evolution. The reconstructed P-T-t evolution indicates a change in metamorphic conditions from M1 ($P = 0.8$–1.0 GPa and $T = 870$–890 °C) to M2 ($P = 0.4$–0.6 GPa and $T = 680$–760 °C), associated with exhumation from deep to middle crustal levels. This corresponds to an increase in the thermal gradient, transitioning from a collisional or post-collisional thermal relaxation setting (27 ± 3 °C/km) to a highly perturbed gradient related to extensional tectonics (40 ± 8 °C/km). The superior precision of CA-ID-TIMS U-Pb zircon dating has been necessary to estimate the time interval between M1 (294.29 ± 0.38 Ma) and M2 (286.76 ± 0.27 Ma), which yields an average exhumation rate of 2.0 ± 1.0 mm/yr.

Comparison with CA-ID-TIMS geochronology from Adriatic rocks in the Alps reveals a magmatic rejuvenation migrating from west to east, confined to the interval 277-294 Ma. This time interval coincides with the intra-continental transtensional phase that affected Pangea during the early Permian (Muttoni et al., 2003), characterized by intense magmatism, volcanism, and HT metamorphism in the deep crust.

CRediT authorship contribution statement

Marco Filippi: Writing – review & editing, Writing – original draft, Visualization, Validation, Supervision, Project administration, Methodology, Investigation, Funding acquisition, Formal analysis, Data curation, Conceptualization. **Federico Farina:** Writing – review & editing, Writing – original draft, Visualization, Validation, Supervision, Resources, Project administration, Methodology, Investigation, Funding acquisition, Formal analysis, Data curation, Conceptualization. **Maria Ovtcharova:** Writing – review & editing, Writing – original draft, Visualization, Validation, Supervision, Resources, Methodology, Investigation, Funding acquisition, Formal analysis, Data curation, Conceptualization. **Fabiola Caso:** Writing – review & editing, Visualization, Investigation, Conceptualization. **Manuel Roda:** Writing – review & editing, Validation, Supervision, Project administration, Funding acquisition, Conceptualization. **Chiara Benedetta Piloni:** Writing – review & editing, Validation, Investigation. **Michele Zucali:** Writing – review & editing, Validation, Supervision, Project administration, Funding acquisition, Conceptualization.

Declaration of competing interest

The authors declare that they have no known competing financial interests or personal relationships that could have appeared to influence the work reported in this article.

Acknowledgements

The work was supported by the Italian Ministry for University and Research (MUR) through the project "Dipartimenti di Eccellenza 2023–27″ and by PRIN2020 through the project "POEM-POligEnetic Mélanges: anatomy, significance and societal impact". We thank Alessandro De Leo for insightful discussions on data treatment.

Supplementary materials

Supplementary material associated with this article can be found, in the online version, at doi:10.1016/j.epsl.2025.119689.

Data availability

All the data are in the supplementary file

References

Baldwin, J.A., Brown, M., 2008. Age and duration of ultrahigh-temperature metamorphism in the Anápolis–Itauçu Complex, Southern Brasília Belt, central Brazil–constraints from U–Pb geochronology, mineral rare earth element chemistry and trace-element thermometry. J. Metamorph. Geol. 26 (2), 213–233.

Baldwin, S.L., Monteleone, B.D., Webb, L.E., Fitzgerald, P.G., Grove, M., June Hill, E., 2004. Pliocene eclogite exhumation at plate tectonic rates in eastern Papua New Guinea. Nature 431 (7006), 263–267.

Barboza, S.A., Bergantz, G.W., 2000. Metamorphism and anatexis in the mafic complex contact aureole, Ivrea Zone, Northern Italy. J. Petrol. 41 (8), 1307–1327.

Bartoli, O., Millonig, L.J., Carvalho, B.B., Marschall, H.R., Gerdes, A., 2024. The age of granulite-facies metamorphism in the Ivrea–Verbano zone (NW Italy) determined through In situ U–Pb dating of garnet. J. Petrol. 65 (8), egae083.

Boscaini, A., Davies, J.H.F.L., Perrot, M.G., et al., 2025. Early permian post-collisional magmatism induced by extensive removal of the Variscan lithospheric mantle. Contrib Miner. Pet. 180, 10.

Bowring, J.F., McLean, N.M., Bowring, S.A., 2011. Engineering cyber infrastructure for U-Pb geochronology: tripoli and U-Pb_Redux. Geochem. Geophys. Geosystems 12 (6).

Caso, F., Strambini, A., Zucali, M., 2024a. Structural, lithostratigraphic and thermal features of a Permian lower crust from the Western Italian Alps (Valpelline Series, Valle d'Aosta). Geol Mag 160 (11), 1983–2009.

Caso, F., Piloni, C.B., Filippi, M., Pezzotta, A., Fazio, E., Visalli, R., Zucali, M., 2024b. Combining traditional and quantitative multiscale structural analysis to reconstruct the tectono-metamorphic evolution of migmatitic basements: the case of the Valpelline Series, Dent-Blanche Tectonic System, Western Alps. J. Struct. Geol. 182, 105099.

Cavalcante, C., Hollanda, M.H., Vauchez, A., Kawata, M., 2018. How long can the middle crust remain partially molten during orogeny? Geology. 46 (10), 839–842.

Condon, D.J., Schoene, B., McLean, N.M., Bowring, S.A., Parrish, R.R., 2015. Metrology and traceability of U–Pb isotope dilution geochronology (EARTHTIME Tracer Calibration Part I). Geochim. Cosmochim. Acta 164, 464–480. https://doi.org/10.1016/j.gca.2015.05.026.

Condon, D., Schoene, B., Schmitz, M., Schaltegger, U., Ickert, R.B., Amelin, Y., Yin, Q.Z., 2024. Recommendations for the reporting and interpretation of isotope dilution U-Pb geochronological information. Geol. Soc. Am. 136 (9–10), 4233–4251.

Connop, C.H., Smye, A.J., Garber, J.M., Moser, A.C., Caddick, M.J., Vervoort, J.D., 2024. Assembly of lower continental crust: a garnet Lu-Hf petrochronological investigation of the Ivrea-Verbano Zone. Italy, Earth Planet. Sci. Lett. 634, 118677.

Crisp, L.J., Berry, A.J., Burnham, A.D., Miller, L.A., Newville, M., 2023. The Ti-in-zircon thermometer revised: the effect of pressure on the Ti site in zircon. Geochim. Cosmochim. Acta 360, 241–258.

Diener, J.F., White, R.W., Link, K., Dreyer, T.S., Moodley, A., 2013. Clockwise, low-P metamorphism of the Aus granulite terrain, southern Namibia, during the mesoproterozoic Namaqua Orogeny. Precambrian. Res. 224, 629–652.

Engi, M., Lanari, P., Kohn, M.J., 2017. Significant ages—An introduction to petrochronology. Rev. Mineral. Geochem. 83 (1), 1–12.

England, P.C., Thompson, A.B., 1984. Pressure—Temperature—Time paths of regional metamorphism I. Heat transfer during the evolution of regions of thickened continental crust. J. Petrol. 25 (4), 894–928.

Ewing, T.A., Hermann, J., Rubatto, D., 2013. The robustness of the Zr-in-rutile and Ti-in-zircon thermometers during high-temperature metamorphism (Ivrea-Verbano Zone, northern Italy). Contrib. Mineral. Petrol. 165, 757–779.

Ewing, T.A., Rubatto, D., Lemke, K., Hermann, J., 2023. Timescales and mechanisms of felsic lower continental crust formation: insights from U-Pb geochronology of detrital zircon (Malenco Unit, eastern Central Alps). Lithos. 456, 107286.

Gaynor, S.P., Ruiz, M., Schaltegger, U., 2022. The importance of high precision in the evaluation of U-Pb zircon age spectra. Chem, Geol 603, 120913.

Guergouz, C., Martin, L., Vanderhaeghe, O., Thébaud, N., Fiorentini, M., 2018. Zircon and monazite petrochronologic record of prolonged amphibolite to granulite facies metamorphism in the Ivrea-Verbano and Strona-Ceneri Zones, NW Italy. Lithos. 308, 1–18.

Harley, S.L., Kelly, N.M., Möller, A., 2007. Zircon behaviour and the thermal histories of mountain chains. Elements 3 (1), 25–30.

Harley, S.L., 2016. A matter of time: the importance of the duration of UHT metamorphism. J. Mineral. Petrol. Sci. 111 (2), 50–72.

Hermann, J., Rubatto, D., 2003. Relating zircon and monazite domains to garnet growth zones: age and duration of granulite facies metamorphism in the Val Malenco lower crust. J. Metamorph. Geol. 21 (9), 833–852.

Holland, T.J., Powell, R., 2011. An improved and extended internally consistent thermodynamic dataset for phases of petrological interest, involving a new equation of state for solids. J. Metamorph. Geol. 29, 333–383.

Horstwood, M.S., Košler, J., Gehrels, G., Jackson, S.E., McLean, N.M., Paton, C., Schoene, B., 2016. Community-derived standards for LA-ICP-MS U-(Th-) Pb geochronology–Uncertainty propagation, age interpretation and data reporting. Geostand. Geoanalytical Res. 40 (3), 311–332.

Jiao, S., Brown, M., Mitchell, R.N., Chowdhury, P., Clark, C., Chen, L., Guo, J., 2023. Mechanisms to generate ultrahigh-temperature metamorphism. Nat. Rev. Earth. Environ. 4 (5), 298–318.

Karakas, O., Wotzlaw, J.F., Guillong, M., Ulmer, P., Brack, P., Economos, R., Bachmann, O., 2019. The pace of crustal-scale magma accretion and differentiation beneath silicic caldera volcanoes. Geology. 47 (8), 719–723.

Kasbohm, J., Schoene, B., Burgess, S., 2021. Radiometric constraints on the timing, tempo, and effects of large igneous province emplacement. Large Igneous Prov.: Driv. Glob. Environ. Biot. Chang. 27–82.

Klötzli, U.S., Sinigoi, S., Quick, J.E., Demarchi, G., Tassinari, C.C., Sato, K., Günes, Z., 2014. Duration of igneous activity in the Sesia Magmatic System and implications for high-temperature metamorphism in the Ivrea–Verbano deep crust. Lithos. 206, 19–33.

Kohn, M.J., 2016. Metamorphic chronology—A tool for all ages: past achievements and future prospects. Am. Mineral. 101 (1), 25–42.

Kunz, B.E., White, R.W., 2019. Phase equilibrium modelling of the amphibolite to granulite facies transition in metabasic rocks (Ivrea Zone, NW Italy). J. Metamorph. Geol. 37 (7), 935–950.

Kunz, B.E., Manzotti, P., von Niederhäusern, B., Engi, M., Darling, J.R., Giuntoli, F., Lanari, P., 2018a. Permian high-temperature metamorphism in the Western Alps (NW Italy). Int. J. Earth. Sci. 107, 203–229.

Kunz, B.E., Regis, D., Engi, M., 2018b. Zircon ages in granulite facies rocks: decoupling from geochemistry above 850 °C? Contrib. Mineral. Petrol. 173, 1–21.

Langone, A., Zanetti, A., Daczko, N.R., Piazolo, S., Tiepolo, M., Mazzucchelli, M., 2018. Zircon U-Pb dating of a lower crustal shear zone: a case study from the northern sector of the Ivrea-Verbano Zone (Val Cannobina, Italy). Tectonics. 37 (1), 322–342.

Lardeaux, J.M., Spalla, M.I., 1991. From granulites to eclogites in the Sesia zone (Italian Western Alps): a record of the opening and closure of the Piedmont ocean. J. Metamorph. Geol. 9 (1), 35–59.

Lenardic, A., Jellinek, A.M., Foley, B., O'Neill, C., Moore, W.B., 2016. Climate-tectonic coupling: variations in the mean, variations about the mean, and variations in mode. J. Geophys. Res.: Planets 121 (10), 1831–1864.

Manzotti, P., Rubatto, D., Zucali, M., Korh, A.E., Cenki-Tok, B., Ballevre, M., Engi, M., 2018. Permian magmatism and metamorphism in the Dent Blanche nappe: constraints from field observations and geochronology. Swiss. J. Geosci. 111, 79–97.

Mattinson, J.M., 2005. Zircon U–Pb chemical abrasion ("CA-TIMS") method: combined annealing and multi-step partial dissolution analysis for improved precision and accuracy of zircon ages. Chem. Geol. 220 (1–2), 47–66.

Muttoni, G., Kent, D.V., Garzanti, E., Brack, P., Abrahamsen, N., Gaetani, M., 2003. Early permian pangea 'B'to late permian pangea 'A'. Earth Planet, Sci, Lett 215 (3–4), 379–394.

Petri, B., Mohn, G., Skrzypek, E., Mateeva, T., Galster, F., Manatschal, G., 2017. U–Pb geochronology of the Sondalo gabbroic complex (Central Alps) and its position within the permian post-variscan extension. Int. J. Earth. Sci. 106, 2873–2893.

Powell, R., Holland, T.J.B., 2008. On thermobarometry. J. Metamorph. Geol. 26 (2), 155–179.

Quick, J.E., Sinigoi, S., Peressini, G., Demarchi, G., Wooden, J.L., Sbisà, A., 2009. Magmatic plumbing of a large Permian caldera exposed to a depth of 25 km. Geology. 37 (7), 603–606.

Ring, U., Brandon, M.T., Willett, S.D., Lister, G.S., 1999. Exhumation processes. *Geological Society*, 154. Special Publications, London, pp. 1–27.

Roda, M., Zucali, M., Li, Z.X., Spalla, M.I., Yao, W., 2018. Pre-alpine contrasting tectono-metamorphic evolutions within the Southern Steep Belt, Central Alps. Lithos. 310, 31–49.

Roda, M., Regorda, A., Spalla, M.I., Marotta, A.M., 2019. What drives Alpine Tethys opening? Clues from the review of geological data and model predictions. Geol. J. 54 (4), 2646–2664.

Rubatto, D., Hermann, J., 2001. Exhumation as fast as subduction? Geology. 29 (1), 3–6.

Rubatto, D., Williams, I.S., Buick, I.S., 2001. Zircon and monazite response to prograde metamorphism in the Reynolds Range, central Australia. Contrib. Mineral. Petrol. 140 (4), 458–468.

Rubatto, D., Hermann, J., Buick, I.S., 2006. Temperature and bulk composition control on the growth of monazite and zircon during low-pressure anatexis (Mount Stafford, central Australia). J. Petrol. 47 (10), 1973–1996.

Rubatto, D., Regis, D., Hermann, J., Boston, K., Engi, M., Beltrando, M., McAlpine, S.R., 2011. Yo-yo subduction recorded by accessory minerals in the Italian Western Alps. Nat. Geosci. 4 (5), 338–342.

Rubatto, D., Chakraborty, S., Dasgupta, S., 2013. Timescales of crustal melting in the Higher Himalayan Crystallines (Sikkim, Eastern Himalaya) inferred from trace element-constrained monazite and zircon chronology. Contrib. Mineral. Petrol. 165, 349–372.

Schaltegger, U., Brack, P., 2007. Crustal-scale magmatic systems during intracontinental strike-slip tectonics: U, Pb and Hf isotopic constraints from permian magmatic rocks of the Southern Alps. Int. J. Earth. Sci. 96, 1131–1151.

Schaltegger, U., Schmitt, A.K., Horstwood, M.S.A., 2015. U–Th–Pb zircon geochronology by ID-TIMS, SIMS, and laser ablation ICP-MS: recipes, interpretations, and opportunities. Chem, Geol 402, 89–110.

Schoene, B., Crowley, J.L., Condon, D.J., Schmitz, M.D., Bowring, S.A., 2006. Reassessing the uranium decay constants for geochronology using ID-TIMS U–Pb data. Geochim. Cosmochim. Acta 70 (2), 426–445.

Schoene, B., Latkoczy, C., Schaltegger, U., Günther, D., 2010. A new method integrating high-precision U–Pb geochronology with zircon trace element analysis (U–Pb TIMS-TEA). Geochim. Cosmochim. Acta 74 (24), 7144–7159.

Schuster, R., Stüwe, K., 2008. Permian metamorphic event in the Alps. Geology. 36 (8), 603–606.

Smye, A.J., Lavier, L.L., Zack, T., Stockli, D.F., 2019. Episodic heating of continental lower crust during extension: a thermal modeling investigation of the Ivrea-Verbano Zone. Earth Planet, Sci, Lett 521, 158–168.

Stowell, H., Schwartz, J., Bollen, E., Tulloch, A., Ramezani, J., Klepeis, K., 2022. Timescales and Rates of Intrusive and Metamorphic Processes Determined from Zircon and Garnet in Migmatitic Granulite, 107. American Mineralogist: Journal of Earth and Planetary Materials, Fiordland, New Zealand, pp. 1116–1132.

Taylor, S.R., McLennan, S.M., 1995. The geochemical evolution of the continental crust. Rev. Geophys. 33 (2), 241–265.

Vavra, G., Schaltegger, U., 1999. Post-granulite facies monazite growth and rejuvenation during permian to lower Jurassic thermal and fluid events in the Ivrea Zone (Southern Alps). Contrib. Mineral. Petrol. 134 (4), 405–414.

Vermeesch, P., 2018. IsoplotR: a free and open toolbox for geochronology. Geosci. Front. 9 (5), 1479–1493.

Volante, S., Blereau, E., Guitreau, M., Tedeschi, M., van Schijndel, V., Cutts, K., 2024. Current applications using key mineral phases in igneous and metamorphic geology: perspectives for the future. In: van Schijndel, V., Cutts, K., Pereira, I., Guitreau, M., Volante, S., Tedeschi, M. (Eds.), Minor Minerals, Major Implications: Using Key Mineral Phases to Unravel the Formation and Evolution of Earth's Crust, 537. Geological Society of London, Special Publications, pp. 57–121.

White, R.W., Powell, R.O.G.E.R., Holland, T.J.B., Johnson, T.E., Green, E.C.R., 2014. New mineral activity–composition relations for thermodynamic calculations in metapelitic systems. J. Metamorph. Geol. 32 (3), 261–286.

Whitehouse, M.J., Platt, J.P., 2003. Dating high-grade metamorphism—Constraints from rare-earth elements in zircon and garnet. Contrib. Mineral. Petrol. 145, 61–74.

Whitney, D.L., Evans, B.W., 2010. Abbreviations for names of rock-forming minerals. Am. Mineral. 95 (1), 185–187.

Wiedenbeck, M., Hanchar, J.M., Peck, W.H., Sylvester, P., Valley, J., Whitehouse, M., Kronz, A., Morishita, Y., Nasdala, L., Fiebig, J., Franchi, I., Girard, J.P., Greenwood, R.C., Hinton, R., Kita, N., Mason, P.R.D., Norman, M., Ogasawara, M., Piccoli, P.M., Rhede, D., Satoh, H., Schulz-Dobrick, B., Skår, O., Spicuzza, M., Terada, K., Tindle, A., Togashi, S., Vennemann, T., Xie, Q., Zheng, Y.F., 2004. Further characterisation of the 91500 zircon crystal. Geostand. Geoanalytical Res. 28 (1), 9–39.

Wolfram, L.C., Weinberg, R.F., Nebel, O., Hamza, K., Hasalová, P., Míková, J., Becchio, R., 2019. A 60-myr record of continental back-arc differentiation through cyclic melting. Nat. Geosci. 12 (3), 215–219.

Wyatt, D.C., Smye, A.J., Garber, J.M., Hacker, B.R., 2022. Assembly and tectonic evolution of continental lower crust: monazite petrochronology of the Ivrea-Verbano Zone (Val Strona di Omegna). Tectonics. 41 (3), e2021TC006841.

Xiang, H., Connolly, J.A., 2022. GeoPS: an interactive visual computing tool for thermodynamic modelling of phase equilibria. J. Metamorph. Geol. 40 (2), 243–255.